UNIVERSITY OF
BATH

University of Bath

ARTICLE OPEN

Identifying light impurities in transition metal dichalcogenides: the local vibrational modes of S and O in ReSe$_2$ and MoSe$_2$

Lewis S. Hart[1], James L. Webb[1], Stephen Murkin[1], Daniel Wolverson[1] and Der-Yuh Lin[2]

The transition metal dichalcogenides provide a rich field for the study of two-dimensional materials, with metals, semiconductors, superconductors and charge density wave materials being known. Members of this family are typically hexagonal, but those based on rhenium (ReSe$_2$ and ReS$_2$) and their ternary alloys are attracting attention due to their triclinic structure and their resulting, strong in-plane anisotropy. Here, Raman spectra of dilute ReSe$_{2-x}$S$_x$ alloys containing low levels of sulfur ($x \leq 0.25$) were obtained in order to investigate the distribution of substitutional sulfur atoms over the non-equivalent chalcogen sites of the ReSe$_2$ unit cell. Four different Raman bands arising from the local vibrational modes of sulfur atoms were observed, corresponding to these four sites. One local vibrational mode has a substantially in-plane displacement of the sulfur atom, two are partially out-of-plane and one is completely out-of-plane. The interpretation of the experimental data is based on calculations of the lattice dynamics and non-resonant Raman tensors of a model alloy via density functional theory. For comparison, polarization-dependent Raman spectra of pure ReS$_2$ are also presented; a dramatic increase in the Raman cross-section is found for the out-of-plane modes when the excitation polarization is normal to the layers and the light propagates in the layer plane. A similar increase in cross-section is found experimentally for the local vibrational modes of sulfur in dilute ReSe$_{2-x}$S$_x$ alloys and is predicted for dilute sulfur-containing alloys based on MoSe$_2$. The analogous local vibrational modes of substitutional oxygen impurities in ReSe$_2$ were also investigated computationally.

npj 2D Materials and Applications (2017)1:41 ; doi:10.1038/s41699-017-0043-1

INTRODUCTION

Rhenium disulfide (ReS$_2$) and rhenium diselenide (ReSe$_2$) have attracted considerable recent attention because of their unusual structure. They belong to the transition metal dichalcogenide (TMD) family reported by Wilson and Yoffe[1] but, unlike more well-known TMDs, their structure is highly anisotropic in the layer plane and this is reflected in all their physical properties.[2–4] The class of van der Waals layered semiconductors with in-plane anisotropy is a topic of great current interest and, besides ReS$_2$ and ReSe$_2$, it includes black phosphorus,[5–7] GeS,[8] transition metal trichalcogenides[9] and Sb$_2$Se$_3$.[10] Proposed applications of ReX$_2$ ($X=$ S, Se) include plasmonic materials,[11] polarization-sensitive photodetectors with high sensitivity,[12–15] inverters,[16] catalytic devices,[17,18] and few-layer field effect[19,20] or heterojunction[21] transistor structures.

The anisotropy of the ReX$_2$ compounds arises because, instead of adopting the octahedral (2H) or trigonal (1T) polymorphs typical of TMDs, they undergo a distortion to form a trigonal 1T′ polymorph.[22] The rhenium atoms are bonded to each other to form diamond-like chains, with the direction of the chains defined here as the a direction[23] (Supplementary Fig. S1). The inter-layer coupling is unusually weak compared to other TMDs,[24–26] though recent angle-resolved photoemission spectroscopy (ARPES) studies show that the band structure of the bulk ReX$_2$ family still has a three-dimensional character.[27–30] ReSe$_2$ is an indirect band gap semiconductor for all numbers of layers[31–34] with a band gap of 1.36 eV[34] whilst there is disagreement as to the nature of the band

gap for bulk ReS$_2$, with some groups reporting an indirect band gap of 1.41 eV and others claiming a direct band gap of 1.5 eV.[31–36]

In this paper, we focus on the alloys of composition ReSe$_{2-x}$S$_x$. These alloys are of interest for two major reasons. Firstly, by changing the composition of sulfur within these alloys it is possible to tune the band gap,[32,37] as found for other TMD alloys[38] and alloys can be produced over the whole composition range, with the anisotropic trigonal structure being preserved throughout. Secondly, the more well-known TMDs exhibit strong spin-orbit splittings (SOS) in the valence band, with the magnitude of this SOS being 180 meV at the K and K' points of the Brillouin zone for bulk MoS$_2$.[39] ReSe$_2$ has space group p$\bar{1}$, with inversion symmetry even for monolayers and thus its spin-orbit splitting is expected to be zero throughout the Brillouin zone. However, DFT calculations with and without the inclusion of spin-orbit coupling (SOC) show that the SOC of the rhenium d bands still perturbs the band structure of ReSe$_2$ significantly.[40] By introducing a sulfur impurity, the center of inversion is removed; as a result of this symmetry breaking, the host crystal field acts as an asymmetric potential and will lift the spin degeneracy at least locally.[41] Rhenium has a high atomic number (higher than molybdenum and tungsten) and thus the spin-orbit splitting is expected to develop rapidly with this symmetry breaking. However, a random distribution of impurity atoms may effectively restore inversion symmetry if the crystal field averages to zero. It is therefore essential to understand whether particular chalcogen sites are preferred and whether non-equilibrium growth techniques or

[1]Centre for Nanoscience and Nanotechnology, Department of Physics, University of Bath, Bath BA2 7AY, United Kingdom and [2]Department of Electronics Engineering, National Changhua University of Education, Changhua 50007, Taiwan
Correspondence: Lewis S. Hart (l.s.hart@bath.ac.uk) or Daniel Wolverson (d.wolverson@bath.ac.uk)

2

post-growth methods can be used to influence the distribution of sulfur over the possible sites.

Here, we address the key question of how to identify sulfur impurities on the different chalcogen sites in $ReSe_{2-x}S_x$ (Supplementary Fig. S1) and we show that this is possible via Raman spectroscopy. In addition, we consider whether substitutional oxygen impurities on chalcogen sites may be detected by the same method. Because all ternary alloys in the TMD family are of considerable potential interest, we consider also the case of sulfur impurities in a more representative and conventional TMD, $MoSe_2$, for which experimental Raman data already exist, identifying similarities in the structure of the Raman tensors for the impurity local vibrational modes (LVMs) in each case.

$ReSe_2$ has 4 formula units per unit cell (12 atoms) and 36 vibrational normal modes are therefore expected of which 33 have non-zero frequencies at the Brillouin zone center and 18 are Raman-active A_g species. Once the center of inversion is eliminated in a random alloy, all 33 modes become Raman-active in principle. There have been very few Raman studies of sulfur-doped $ReSe_2$[32,42] though Liu et al. reported the Raman spectrum of the ReSeS ternary alloy. However, with 33 modes spread over a range of 100–500 cm^{-1}, the analysis of this spectrum is not trivial.[25] Wen et al. reported Raman spectroscopy of $ReSe_{2-x}S_x$ alloy monolayers suggesting, for low sulfur compositions, that the higher frequency modes disappear.[43] It is shown here that these modes can be observed clearly in dilute alloy samples, and appropriate experimental geometries for this are identified.

RESULTS

Raman scattering of high-frequency vibrational modes of ReS_2

Before considering the alloys, we discuss a useful but uncommon experimental geometry in which the laser excitation propagates in the layer plane. Such "edge-on" spectroscopic experiments have identified out-of-plane vibrational modes in the Raman spectra of other 2D materials[44,45] and the technique can give a better understanding of photoluminescence selection rules.[46] This geometry is particularly valuable for identifying the highest-frequency vibrational mode of $ReSe_{2-x}S_x$; to show this, we consider first the case of pure ReS_2. The Brillouin zone-center phonon modes of ReS_2 include 18 Raman-active modes,[24,47] several of which can be seen in the experimental data of Fig. 1a.

Their intensities I are determined by Raman tensors R according to

$$I \propto |e_i . R . e_s|^2, \tag{1}$$

where e_i and e_s are the incident and scattered light polarization vectors respectively. As in the case of $ReSe_2$, all Raman-active modes in ReS_2 belong to the non-degenerate symmetry species A_g with a Raman tensor R which has only non-zero elements and is given in Cartesian axes in the laboratory frame by

$$R = \begin{pmatrix} u & v & r \\ v & w & s \\ r & s & t \end{pmatrix}. \tag{2}$$

We used a polarization-insensitive spectrometer with no analyzer before the detector.[48] Then, with propagation of light along the normal to the layer plane (i.e, along z in the coordinate system of equation 2), the Raman scattering of intensity I a given mode is

$$I = u^2 \cos^2 \theta + w^2 \sin^2 \theta + v^2 + 2v(u+w)\sin \theta \cos \theta; \tag{3}$$

θ is the polarization angle of the excitation with respect to the in-plane x direction, here parallel to the rhenium chains and the crystallographic direction a as shown in Fig. 1b. The use of equation 3 to model the angle-dependent Raman scattering of bulk $ReSe_2$ and ReS_2 was tested previously.[48,49]

For ReS_2, the highest-frequency predicted mode (438 cm^{-1}) has a relatively large component t of the Raman tensor R as defined in equation 2 (atomic displacement patterns and numerical values of R are given in Supplementary Fig. S3). Therefore, when the incident light is polarized perpendicular to the layer plane, the 438 cm^{-1} Raman mode will be significantly more intense than for polarization in the layer plane. To test this, we use the "edge-on" geometry with the propagation of light along the crystallographic a direction, Fig. 1c. Analogous to equation 3, the intensity of each Raman band with unpolarized detection now follows the relationship

$$I = t^2 \cos^2 \varphi + w^2 \sin^2 \varphi + s^2 + 2s(w+t)\sin \varphi \cos \varphi \tag{4}$$

for excitation polarized parallel and perpendicular to the layer normal ($\varphi = 0°$ and $\varphi = 90°$ respectively). Figure 1a shows the resulting Raman spectra of ReS_2. The intensities of the lower-frequency modes (from 100 to 400 cm^{-1}) change by less than a factor of two between these two polarizations; however, the intensity of the 438 cm^{-1} mode increases very strikingly at $\varphi = 0°$ and fitting the experimental data gives an enhancement of
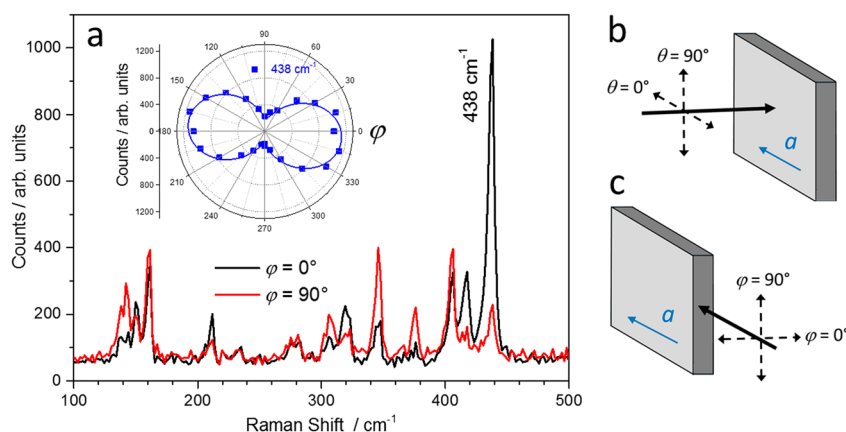
Fig. 1 Enhancement of the Raman signals of ReS_2 in the "edge-on" geometry. **a** Raman spectra of ReS_2 for light polarized parallel ($\varphi = 0°$, black line) and perpendicular ($\varphi = 90°$, red line) to the normal to the layers z with the direction of propagation along the crystallographic a direction (the direction of the rhenium chains). Inset: experimentally-determined (points) and fitted (solid line) dependence of the intensity of the 438 cm^{-1} Raman mode of ReS_2 on the angle φ in this geometry. **b** and **c** Schematic diagrams of the conventional and "edge-on" Raman experiments respectively; the solid black arrows represent the direction of the incident laser beam (back scattered light is detected in both cases) and the dashed arrows define the angles used to specify the laser polarization

$I_{para}/I_{perp} \sim 6$. The true enhancement in this geometry may be even larger, given that the thickness of the flake is comparable to the laser spot size, so that the effective volume of sample is lower in the "edge-on" geometry. The inset to Fig. 1a shows the measured dependence of the intensity of the 438 cm^{-1} Raman signal on the incident polarization angle φ. A fit using equation 4 has been added, showing the predicted two-fold symmetry. Supplementary Fig. S3 shows the simulated angle dependence based on the Raman tensor obtained from DFT calculations, which give a predicted value of $I_{para}/I_{perp} \sim 14$, in reasonable agreement with experiment. Finally, the inset of Fig. 1 shows that the polarization direction at maximum signal is inclined at $6 \pm 1°$ to the normal to the layers; this is also reproduced in the simulated angle-dependence (Supplementary Fig. S3).

These results demonstrate, firstly, that the calculated Raman tensors for the ReS$_2$ system (and the atomic displacements on which they depend) are reliable and, secondly, that the highest-frequency Raman active phonon of ReS$_2$ involves the out-of-plane motion of the sulfur atoms, with a strong Raman cross-section for excitation polarized normal to the layers. ReSe$_2$ shows very similar polarization-dependence for its highest frequency Raman-active mode with predicted and measured $I_{para}/I_{perp} \sim 12$ and 4, respectively (Supplementary Fig. S4).

Lattice dynamics of ReSe$_{1.75}$S$_{0.25}$: computational results

We now turn to alloys dilute enough to display a sulfur LVM in a ReSe$_2$ lattice; this facilitates experimental recognition of this mode, and provides an input for modified random element isodisplacement (MREI) models,[50,51] as applied recently to a range of TMDs.[52–55]

Figure 2 (inset) shows the eight chalcogen sites that substitutional sulfur may occupy in the ReSe$_2$ unit cell. The number of arrangements of r sulfur atoms on the n chalcogen sites of the primitive unit cell (considered as non-equivalent) is given by ^nC_r with $n = 8$. This number should be halved since each configuration has an experimentally-equivalent one related by inversion (Fig. 2, inset). Therefore, for one sulfur atom per unit cell, composition ReSe$_{1.75}$S$_{0.25}$, the sulfur atom can occupy one of only four distinct chalcogen positions; for two sulfur atoms per unit cell, there are 14 non-equivalent arrangements and for three there are 28. It is feasible but computationally expensive to calculate the phonon modes for all these configurations but at low sulfur concentrations this is unnecessary, as follows. Ho et al. concluded from X-ray studies that sulfur in bulk crystals grown by vapor transport is distributed homogenously. If we assume sulfur is randomly distributed with a constant occupation probability of $x/2$ for any chalcogen site, then by the binomial theorem, the probability of r sulfur atoms being within a single unit cell is $P(r) = {}^8C_r (1 - x/2)^{8-r} (x/2)^r$. Thus, for our experimental concentration of one sulfur per eight formula units, $x = 0.125$, $P(0) = 0.60$, $P(1) = 0.32$, $P(2) = 0.07$, and $P(m) < 0.01$ for all $m > 2$. Thus, the most probable unit cell configuration is pure ReSe$_2$ and only ~8% of unit cells contain more than one sulfur atom.

The lattice modes of ReSe$_{1.75}$S$_{0.25}$ were calculated via density functional perturbation theory (DFPT) and Fig. 2 summarizes the results: the frequencies up to the 29th mode are similar to those of ReSe$_2$[49] and are insensitive to the site occupied by sulfur (changes in frequencies vary by less than typical DFPT accuracy, ~2–3%). From the 30th mode upwards, the frequencies diverge from those of ReSe$_2$. The most dramatic change is seen at mode 36, which occurs at four remarkably different frequencies: 350, 390, 410 and 433 cm^{-1}, depending on the site occupied by the sulfur (Fig. 2, right). These frequencies cover a large enough range that Raman spectroscopy should be capable of identifying sulfur in all four sites, in contrast to the case of the binary compound ReSeS, where there are many possible unit cell configurations, so that its Raman bands overlap strongly. The Raman tensors associated with these modes are given in Supplementary Fig. S5, and we compare these to experiment later

Importantly, our LVM calculations are not significantly affected by the use of a small unit cell. We have calculated the frequencies of the phonon modes for a $2 \times 1 \times 1$ and a $2 \times 2 \times 1$ supercell, each containing one sulfur atom (compositions ReSe$_{1.825}$S$_{0.125}$ and ReSe$_{1.9375}$S$_{0.0625}$) and find the spread of high-frequency modes is similar to those calculated for ReSe$_{1.75}$S$_{0.25}$ (frequencies are tabulated in Supplementary Fig. S5, and compared graphically, Fig. S9). We do see small systematic differences in the frequencies of the spatially-extended phonons as the unit cell size changes (Supplementary Fig. S9) as expected since the net chalcogen mass in the supercell is changing.

An important observation is that the predicted frequency of the sulfur LVM at site D (433 cm^{-1}) is extremely close to the highest-
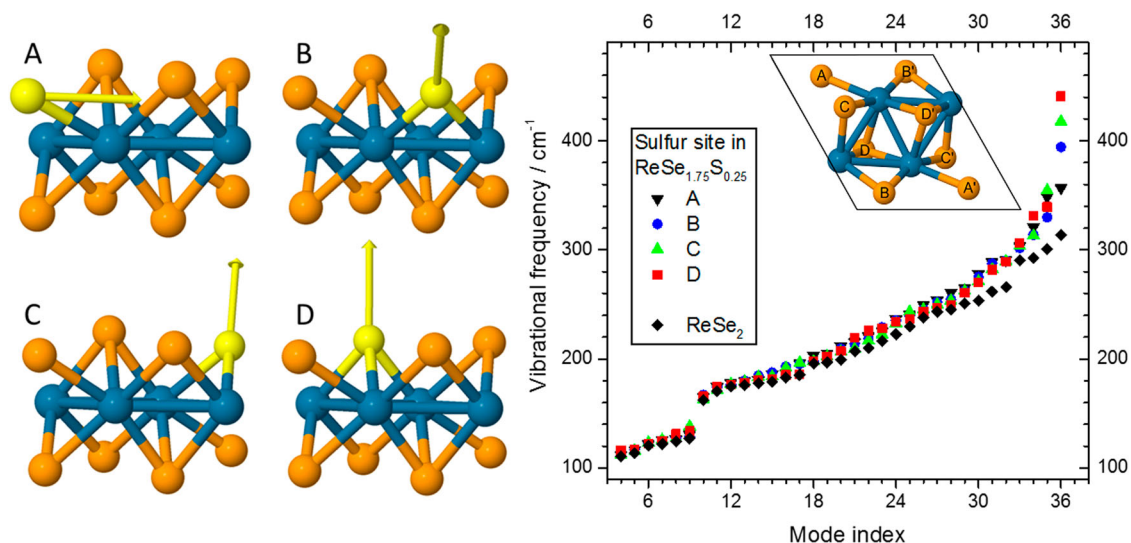
Fig. 2 Local vibrational modes of substitutional S in ReSe$_2$. Left: primitive unit cells of ReSe$_{1.75}$S$_{0.25}$ with a sulfur impurity placed in each of the non-equivalent positions A–D in turn. Yellow arrows show calculated displacements of the atoms in the highest-frequency LVM; those for A and D lie in the plane of the page. Right: calculated frequencies of the zone-center phonon modes (in order of increasing frequency) for a ReSe$_{1.75}$S$_{0.25}$ unit cell with a sulfur atom in each of the sites A–D; the phonon frequencies of ReSe$_2$ are plotted in the same way for comparison. The inset unit cell shows sites A–D viewed normal to the layer and inversion-related sites A′–D′ are also shown

frequency phonon mode of ReS_2 observed in the previous section (438 cm^{-1}). This is not a coincidence; the atomic displacements are related for both modes and predominantly involve the same chalcogen site D (compare Fig. 2 and Fig S1). This phonon branch in ReS_2 is essentially dispersionless; the calculated phonon dispersion for ReS_2[24] shows that the motions of sulfur atoms in neighboring unit cells are not strongly correlated, so that a large supercell is not required. Another way of demonstrating this is that the displacements of neighboring atoms tend to zero rapidly with distance from the sulfur atom, particularly for the D site (Supplementary Fig. S8) so that the high-frequency sulfur vibrational modes are localized and independent of concentration.

We conclude that the highest-frequency LVM of sulfur in $ReSe_2$ is related to the highest-frequency phonon mode of ReS_2 and its predicted frequency is the same to within the typical accuracy of DFPT calculations. Thus, the appearance of this mode in the Raman spectra of $ReSe_{2-x}S_x$ alloys is not evidence of ReS_2 phase segregation, but does indicate the presence of substitutional sulfur. Similar behavior is expected for light substitutional S (and O) impurities in other TMDs, as exemplified next by the case of $MoSe_2$.

Lattice dynamics of $MoSe_{2-x}S_x$: computational results

We now consider the related question of the LVM arising from sulfur as a light impurity in a more conventional, hexagonal TMD, choosing 2H-MoS_xSe_{2-x}, for which experimental Raman studies have been reported.[38,52] Here, only one chalcogen site exists in the primitive unit cell, and localized modes can be of both A or B (out-of-plane, non-degenerate) and E (in-plane, two-fold degenerate) symmetry types.[56] Our findings are summarized in Fig. 3; as in the case of $ReSe_2$, the highest-frequency mode involves an out-of-plane motion of the S impurity whilst other atomic displacements are small. Again, the largest deviation in frequency from the bulk modes of $MoSe_2$ is seen for the highest-frequency modes, though there are now four modes that are strongly distinguished from the host phonons. The highest-frequency sulfur-related mode is non-degenerate (type A), there is a nearly-degenerate pair of in-plane modes, and there is one lower-frequency non-degenerate mode. The highest-frequency sulfur mode is once more above the top of the $MoSe_2$ phonon dispersion, forming an out-of-plane LVM.

Experimental studies of 2H-MoS_xSe_{2-x} showed that the observed phonon frequencies can be described well by an MREI model from which the impurity (local) modes of sulfur in $MoSe_2$
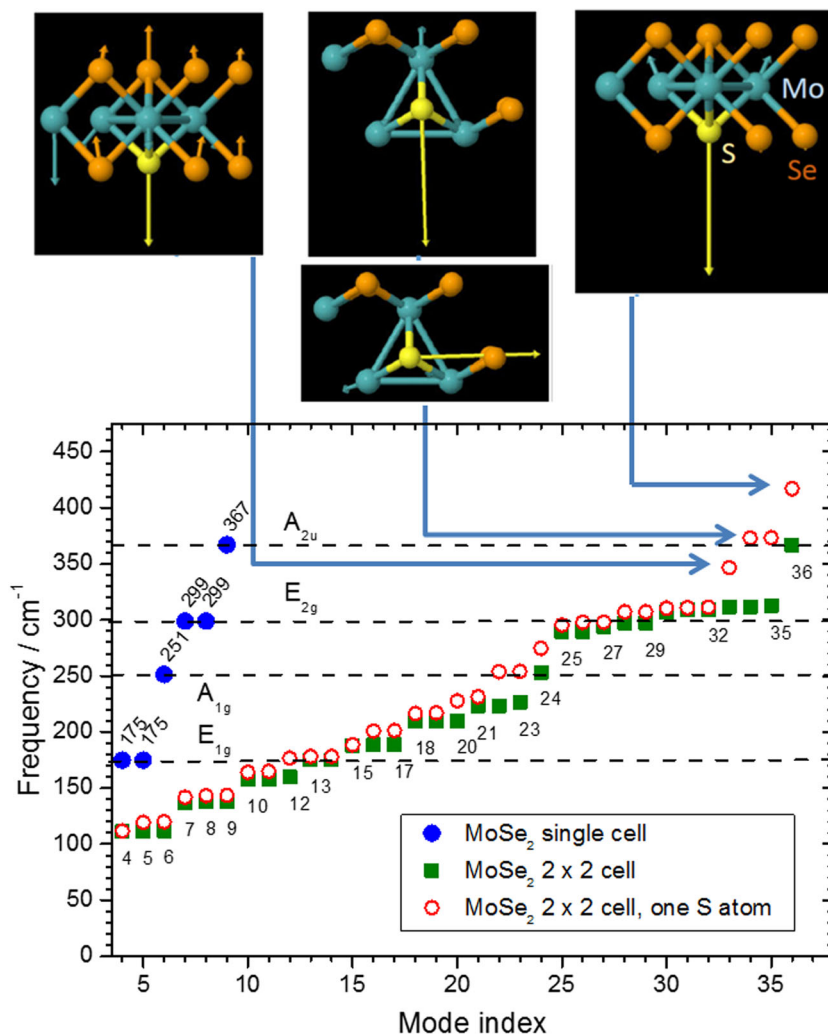
Fig. 3 Local vibrational modes of substitutional S in $MoSe_2$. Top: atomic displacements of the four highest-frequency vibrational modes of monolayer $MoSe_2$ containing one S impurity atom per 12-atom $2 \times 2 \times 1$ supercell ($MoSe_{1.75}S_{0.25}$), calculated via DFPT (vectors are scaled proportionately to the atomic displacement and are drawn for all atoms but some are too small to be seen). Bottom: vibrational frequencies calculated by DFPT for a single $MoSe_2$ unit cell, a $2 \times 2 \times 1$ $MoSe_2$ supercell, and a $2 \times 2 \times 1$ supercell with one Se atom replaced by S. The horizontal dashed lines indicate the symmetry species and the frequencies of the bulk $MoSe_2$ zone-center modes

(adjustable parameters in MREI) were inferred to have frequencies of 343 cm-1 (for the in-plane E_{2g} mode) and 391 cm-1 (A_{1g} mode). These values are in good agreement with those we obtain from DFPT as shown on Fig. 3, which are 367 and 417 cm^{-1} for the E-type modes (34,35) and A-type mode (36), respectively. The agreement is particularly good if we take into account the fact that our calculations for $MoSe_2$ systematically overestimate the phonon frequencies by about 5%, or ~16 cm^{-1} in this frequency range.

These modes were not observed unambiguously at low concentrations in the previous study, although there is some weak structure in the experimental spectra for $x = 0.2$ at around 350–360 cm^{-1} which strengthens and evolves towards the MoS_2 E_{2g} mode with increasing sulfur content.[52] A difficulty in backscattering experiments is that numerous overtone modes fall within the frequency range of the sulfur LVM, for example $E_{1g} + A_{1g}$ and $E_{2g} + LA(M)$.[52] An experiment in the "edge-on" geometry may be able to resolve this. The calculated Raman tensors for modes 33–36 are given in Supplementary Fig. S14 and, for the highest-frequency LVM, t is ~17 times larger than the next largest component of the Raman tensor, so that its "edge-on" signal should be enhanced by up to ~$17^2 = 270$. This agrees qualitatively with data on vertically-aligned MoS_2 layers (for which the backscattering geometry is now "edge-on"), where the intensity of the A_{1g} mode at 408 cm^{-1} increased relative to that of the E_{2g} mode (383 cm^{-1}) in the "edge-on" geometry.[45]

Experimental Raman spectra of $ReSe_{1.875}S_{0.125}$

We now test the above predictions experimentally for a dilute alloy and compare to the pure binary materials, taking $ReSe_{1.875}S_{0.125}$ as a composition that is dilute enough for a true LVM to exist but concentrated enough that signals are easily detected. Measured Raman spectra of $ReSe_2$, $ReSe_{1.875}S_{0.125}$ and ReS_2 are shown in Fig. 4. We note first that we observe bands in the $ReSe_2$ spectrum which have not previously been reported (seen on the left of Fig. 4b). These lie between 320 and 360 cm^{-1} and do not correspond to first-order Raman-active modes of $ReSe_2$.[48] These bands are most probably due to overtones or combinations of phonons, as are known to be observed in some TMDs[57–59] though, owing to the large number of bands (36) in the phonon dispersion of $ReSe_2$, it is difficult to identify the exact branches giving rise to these overtones.

By comparing the alloy spectra to that of $ReSe_2$, we observe four peaks which can be attributed to the substitutional sulfur LVM, which we label A–D; the frequencies of these are shown in Table 1. Peak A is predicted from our DFPT calculations to be at 350 cm^{-1} and there is indeed a peak in the Raman spectra of the alloy near this position (345 cm^{-1}); however, this overlaps with a broad band in the $ReSe_2$ spectrum, and so it is not possible to attribute this peak unambiguously to a LVM. The other three Raman bands of the alloy, B–D, are expected from calculations of their Raman tensors (Supplementary Fig. S5) to be more intense than band A, and are observed in a region of the Raman spectra where there are no modes of the pure material (Fig. 4a, b), so their
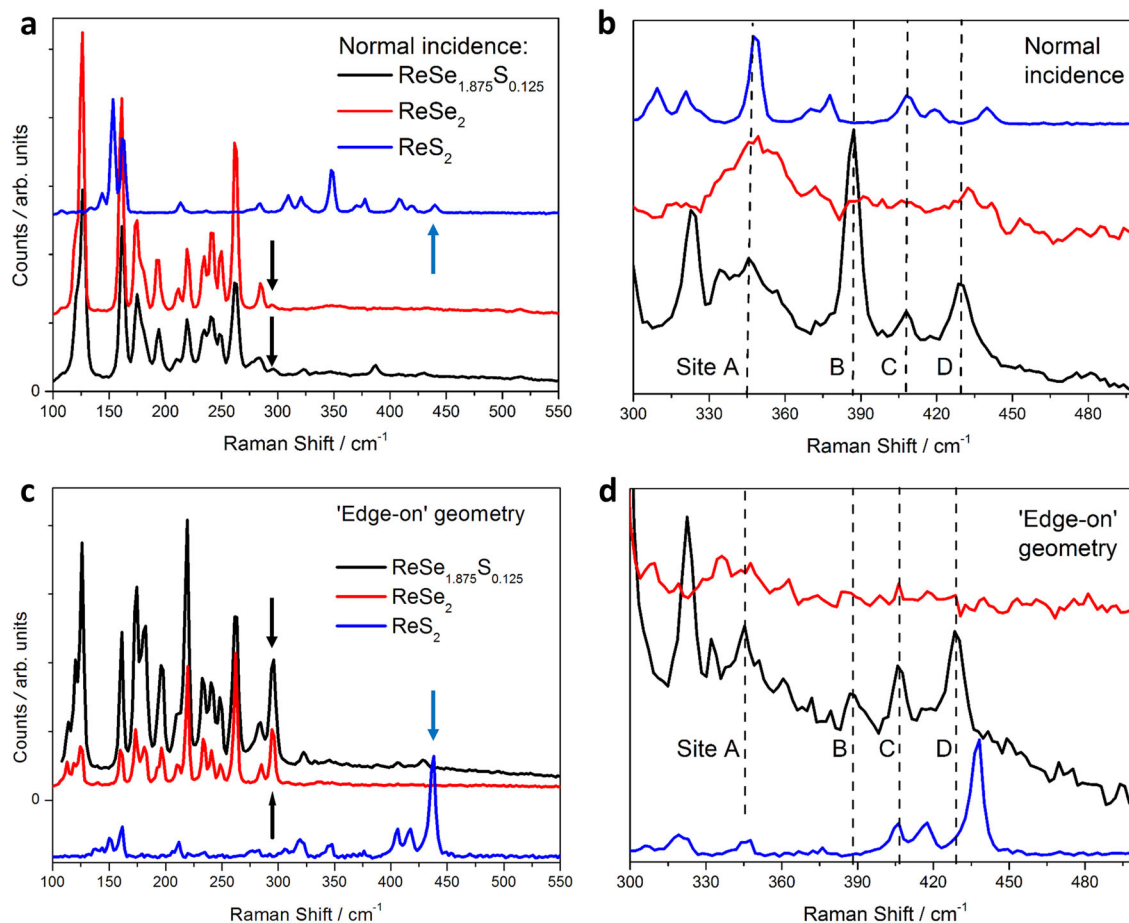
Fig. 4 Experimental Raman spectra of ReS_2, $ReSe_2$, and $ReSe_{1.875}S_{0.125}$. **a** Raman spectra for excitation normal to the layers and the incident polarization in-plane and perpendicular to the a direction; **b** Raman spectra as in **a** but showing the high frequency region on an expanded scale; **c** Raman spectra recorded using the "edge-on" geometry with the incident polarisation normal to the layers; **d** Raman spectra in the "edge-on" geometry as in **c** in the frequency region of the LVMs. Spectra are displaced vertically for clarity. Vertical arrows in **a** and **c** indicate the highest-frequency phonon modes of pure $ReSe_2$ (296 cm^{-1}) and ReS_2 (438 cm^{-1})

Table 1. Calculated and experimental frequencies for the highest-frequency Raman mode of substitutional sulfur impurities on the four non-equivalent sites A–D in $ReSe_2$ (Supplementary Fig. S1)

Sulfur site	Frequency (cm^{-1})			
	DFT, single cell (12 atoms) $ReSe_{1.75}S_{0.25}$	DFT, supercell doubled along a $ReSe_{1.875}S_{0.125}$	DFT, supercell doubled along a, b $ReSe_{1.9375}S_{0.0625}$	Experiment $ReSe_{1.875}S_{0.125}$
A	350	356	347	345*
B	390	396	386	386
C	410	416	417	408
D	433	438	437	429

The experimental band marked * coincides with an overtone Raman band of $ReSe_2$

identification is clear. There is also a strong peak at 322 cm^{-1}, close to the frequencies of the 34th and 35th alloy modes, which is particularly strong in this geometry. This mode almost certainly arises from the incorporation of sulfur since it is not seen in $ReSe_2$ but, because the 34th and 35th modes are so close-lying for the different sulfur sites A–D, it is difficult to assign this peak to a specific site or mode with certainty (Fig. 2 shows that these modes are closely grouped between 310 to 350 cm^{-1}). However, the agreement of these observations with DFPT results (shown in Table 1) to well within the limits of error (here, a ~3% overestimate) gives us confidence in the assignment of at least three of the four highest-frequency Raman bands to sulfur LVMs. Table 1 includes calculated results with three supercells, giving sulfur concentrations above, below and equal to the experimental concentration; the results do not vary significantly, as expected of an LVM. Supplementary Fig. S9 gives further comparison of the results for different supercells.

The highest-frequency vibration was predicted above to have a large out-of-plane displacement and a large element t in its Raman tensor (Eq. 2). Therefore this mode should give a strong signal for incident light polarized perpendicular to the layer. To test this, Raman spectra were obtained in the "edge-on" geometry as for ReS_2 above; results are shown in Fig. 4c, d). Using this geometry, these modes are clearly identifiable, demonstrating that this experimental technique allows for the identification of the highest vibrational mode of lightly sulfur doped $ReSe_2$. The Raman tensors, normal incidence θ-dependence and "edge-on" φ-dependence of bands A–D are presented in Supplementary Figs. S5, S6 and S7 and, as found experimentally, our calculations predict that the near in-plane mode B is stronger than band D for polarization in the layer plane and normal to a (see Fig. 4b, S7) whilst D is stronger than B for polarization normal to the layers (see Fig. 4d, S5).

One comment concerns the frequencies of the spatially extended phonon modes (below 300 cm^{-1}) for the alloy, Fig. 4a, c. Fitting of these spectra reveals that all bands shift to higher frequency by about 1% with respect to the corresponding modes of $ReSe_2$, confirming the incorporation of sulfur. This shift is known[43] and, over the whole composition range, is approximately linear. It is reproduced in our calculations and is principally accounted for by the mass difference of the chalcogen atoms[47] though, interestingly, the sulfur site plays a role; the calculated shifts of representative lattice modes (Supplementary Fig. S10) are dependent on the location of sulfur atom (Supplementary Figs. S11 and S12). We chose modes #9 and #10 (124.8 and 159.7 cm^{-1} in $ReSe_2$) for this, and we used their calculated atomic displacement patterns to identify the analogous modes in the alloy (Supplementary Fig. S10). Thus, interpolation between the binary compounds can only be used to infer composition from alloy mode frequencies if some assumption is made about the distribution of sulfur over sites A-D, such as the random distribution normally assumed in MREI.[52,55]

Oxygen impurities in $ReSe_2$: computational results

It is interesting to ask whether oxygen can form a similar substitutional impurity to sulfur, either via contamination during bulk crystal growth in silica or via atmospheric oxidation. Previous computational studies have investigated oxygen incorporated into ReX_2, either as substitutional atomic O[60] or molecular O_2, and have studied the resulting electronic band structure. Here, we investigate what vibrational modes would be expected from substitutional oxygen impurities; this is important for our understanding of the dilute alloys with sulfur in order to establish that the LVMs we observe are not due, for example, to native oxide at the surface. Figure 5 shows that the highest vibrational mode again has four frequencies corresponding to oxygen occupying sites A–D and these lie in a different range to those of sulfur. The displacement patterns are, however, similar to those of sulfur and the Raman tensors again have large components for polarization normal to the layers.

We annealed $ReSe_2$ in air with times and temperatures following a previous work,[61] where X-ray photoelectron spectroscopy (XPS) revealed surface oxidation. However, we did not observe any oxygen-related modes, presumably because Raman is not as surface-sensitive as XPS and the total quantity of oxide is small. There are reports of the Raman spectra of Re oxides, including partially oxidized ReS_2 containing ReO_3,[62] pure ReO_3[63,64] and Re_2O_7,[50,65,66] but neither of these oxides possesses a configuration analogous to the O atom bridging three Re atoms (site D) that provides the highest frequency LVM here, and neither shows strong Raman bands in the region of 450 to 650 cm^{-1}. It is not our aim here to investigate all configurations of oxygen in $ReSe_2$ and, certainly, more substantial structural modifications and also the role of chalcogen vacancies[67,68] should be considered.

In summary, the LVMs observed in dilute sulfur alloys cannot be attributed to oxygen, and we do not detect significant oxidation of micron-scale flakes even after annealing. However, our results provide a means of identifying the specific configuration of a substitutional oxygen atom on a $ReSe_2$ chalcogen site.

DISCUSSION

The frequencies of the LVMs of substitutional oxygen and sulfur atoms on the four non-equivalent chalcogen sites A–D of $ReSe_2$ have been identified computationally and those of sulfur have been verified experimentally. The four LVMs of sulfur have remarkably different frequencies, providing a means of monitoring the occupation of these sites in $ReSe_{2-x}S_x$ alloys. Analogous behavior has been predicted for the cases of oxygen impurities in $ReSe_2$ and sulfur impurities in $MoSe_2$. The relationship between the $ReSe_{2-x}S_x$ LVMs and the highest-frequency phonon mode of ReS_2 has also been demonstrated. The agreement between experimental and computational results extends also to the enhanced Raman scattering cross-sections when the experimental geometry is chosen so that the light propagates in the layer plane,
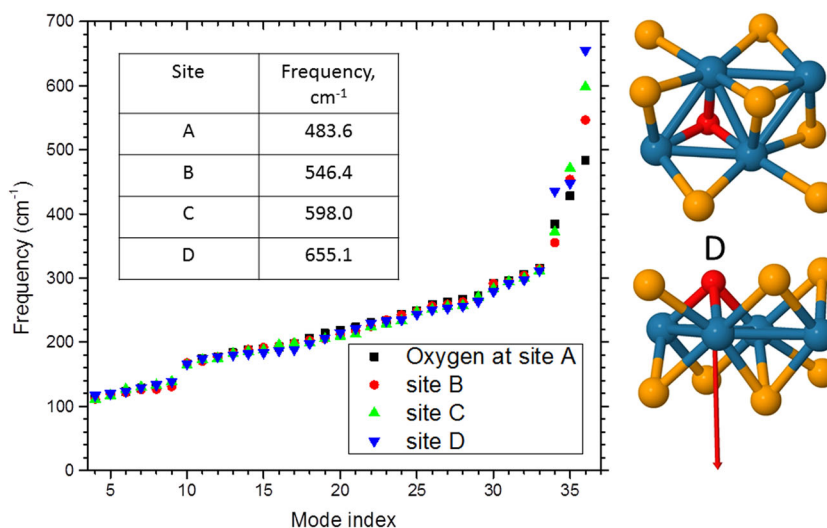
Fig. 5 Local vibrational modes of substitutional O in ReSe$_2$. Left: calculated phonon frequencies of the zone center modes for ReSe2 with one substitutional oxygen atom per unit cell, placed on each of the sites A–D. Right: The unit cell with oxygen at site D, viewed normal (top) and edge-on (bottom) to the layer; the red arrow indicates the displacement of the oxygen atom in the 655.1 cm^{-1} mode (index 36)

which is predicted from the non-resonant Raman tensors. This effect has been demonstrated in Raman spectroscopic studies of both ReS$_2$ and a dilute ReSe$_{2-x}$S$_x$ alloy and is predicted for MoSe$_{2-x}$S$_x$. In a dilute alloy sample, all four LVMs were observed, though the identification of the band arising from site A was tentative since it overlaps an overtone band of ReSe$_2$. The observation of all four predicted bands suggests a random distribution of substitutional sulfur impurities in bulk alloys grown by vapor transport.

METHODS

The ReS$_2$ crystals were supplied by 2D Semiconductors, CA, and have a purity of 99.9995% characterized by secondary ion mass spectroscopy. ReSe$_2$ samples were supplied by HQgraphene, Netherlands. A sulfur-containing ReSe$_2$ sample with a nominal composition of ReSe$_{1.9}$S$_{0.1}$ was grown via chemical vapor transport following the technique described by Huang et al.[69] and energy-dispersive X-ray analysis (EDX) indicated a sulfur concentration of ~1 sulfur atom per 8 formula units (ReSe$_{1.875}$S$_{0.125}$), consistent with the nominal composition. EDX results also suggested a small chalcogen deficiency in this sample, as found by Ho et al.[42] From EDX in imaging mode, a uniform distribution of sulfur was found on a macroscopic scale (Supplementary Fig. S13). Synchrotron-based ARPES studies of the binary compounds and associated XPS measurements[28,29] revealed no significant impurities except for native surface oxide for samples cleaved in air. Samples cleaved in UHV did not show the presence of oxygen. Thick (micron-scale) flakes of the rhenium dichalcogenides were exfoliated using blue Nitto tape and placed onto Gel-Film® WF 6.0 mil in order to perform out-of-plane Raman measurements. To explore the effects of oxygen incorporation, samples were annealed in air following the procedure reported for ReS$_2$,[61] but no changes were observed in the Raman spectra. Small changes in the lower-frequency ReS$_2$ phonons were reported after exposure to O$_2$ plasma,[62] but this was coupled with the appearance of ReO$_3$ in XPS spectra, rather than substitutional oxygen.

Raman spectra were recorded using a Renishaw inVia Raman microscope with a 50× lens with a spatial resolution of ~1 μm. A 532 nm laser was used for all the results presented here and the intensity was kept below 300 μW. No polarization analyzer was used; the detector was previously demonstrated to be polarization insensitive for Raman shifts below 500 cm^{-1}.[48] For "edge-on" measurements, thick flakes were exfoliated onto Gel-Pak film using micromechanical exfoliation. A single crystal flake partially suspended from the edge of the film was then identified (Supplementary Fig. S2) and the sample was placed upon a support to orient it easily. It would be challenging to observe the signals we discuss below in few-layer structures but suitable structures could be

prepared by exfoliation onto graphite, supporting the resulting heterostructure in the same way as above.

Data presented here were obtained with a photon energy of 2.33 eV, above the excitonic band gaps of ReSe$_2$ and ReS$_2$ (1.3–1.6 eV, discussed above), so we do not expect strong resonant or optical interference effects in the Raman scattering. Spectra obtained using 1.58 eV excitation (above the band gap of ReSe$_2$ but close to that of ReS$_2$) did not show significant changes at room temperature though we observe clear resonant effects in the Raman scattering of bulk ReS$_2$ at low temperatures in the energy range of its excitonic transitions (results will be presented elsewhere).

Phonon modes of all materials were calculated using DFPT using a plane wave basis as implemented in the Quantum Espresso code.[70,71] Calculation of the non-resonant Raman tensors necessitated the use of norm-conserving pseudopotentials; the valence of Re was taken as 7 with atomic configuration 5d^5 6 s^2 and a local density approximation-correlation functional was used of the PZ form.[72] Convergence of the total energy was checked with respect to the kinetic energy cutoff (60 Rydberg) and the Monkhorst-Pack k-point grid[73] for a 12-atom unit cell of (8 × 8 × 8). Bulk, three-dimensional material was simulated with three different cell sizes; 12-atoms, 24-atoms and 48-atoms, corresponding to the primitive unit cell and cells doubled along one or both in-plane dimensions. In each case, one S atom was introduced, with separate calculations being made for each of the four non-equivalent chalcogen positions. This gave effective concentrations of twice, equal to, and half of the experimental concentration of S. Initial unit cell parameters and atomic coordinates were taken from Lamfers et al.[23] or Ho et al.[32] with similar results; these were relaxed to obtain atomic forces less than 10^{-3} eV/Å. Similar criteria gave good agreement for the phonons of other TMDs.[74,75] The atomic configuration in the vicinity of the S impurity undergoes significant relaxation in order to shorten the Re-S bond distance (e.g, to 2.33 Å compared to a distance of 2.45 Å for a Se atom on the same site). The resulting structure is stable, with no imaginary phonon frequencies. Calculated frequencies were overestimated by up to 2–3% compared to experiment, typical of the above methodology, and confirmed by our experimental results for ReS$_2$ and ReSe$_2$. The crystal structures were drawn using the Jmol or XCrysden packages.[76]

It is beyond our present scope to consider the dependence of the phonons on layer thickness, but studies of ReS$_2$[77,78] and ReSe$_2$[48,79] as well as Re(S,Se)$_2$[43] show that the phonons shift only weakly in frequency with thickness down to the monolayer level. For the LVMs that are our focus, we find no significant dependence on unit cell size.

Data availability
Data that supports the findings of this study is available from the University of Bath archive (DOI: 10.15125/BATH-00373)

AUTHOR CONTRIBUTIONS

L.S.H. carried out the experimental Raman studies and was first author of the paper; S.M., J.L.W. and D.W. carried out the computational modeling and L.S.H., J.L.W., and D.W. analyzed the data. D.Y.L. grew and characterized the alloy crystals used and all authors discussed the results and contributed to the final version of the paper.

ADDITIONAL INFORMATION

Supplementary information accompanies the paper on the *npj 2D Materials and Applications* website (https://doi.org/10.1038/s41699-017-0043-1).

Competing interests: The authors declare that they have no competing financial interests.

Publisher's note: Springer Nature remains neutral with regard to jurisdictional claims in published maps and institutional affiliations.

REFERENCES

1. Wilson, J. A. & Yoffe, A. D. Transition metal dichalcogenides discussion and interpretation of observed optical, electrical and structural properties. *Adv. Phys.* **18**, 193–335 (1969).
2. Rahman, M., Davey, K. & Qiao, S. Z. Advent of 2D rhenium disulfide (ReS2): fundamentals to applications. *Adv. Funct. Mater.* **27**, 1606129 (2017).
3. Hafeez, M., Gan, L., Saleem Bhatti, A. & Zhai, T. Rhenium dichalcogenides (ReX2, X = S or Se): an emerging class of TMDs family. *Mater. Chem. Front.* **1**, 1917–1932 (2017).
4. Ho, C. H., Huang, Y. S. & Tiong, K. K. In-plane anisotropy of the optical and electrical properties of ReS2 and ReSe2 layered crystals. *J. Alloys Compd.* **317**, 222–226 (2001).
5. Wang, Y. et al. Remarkable anisotropic phonon response in uniaxially strained few-layer black phosphorus. *Nano Research* **8**, 3944–3953 (2015).
6. Ribeiro, H. B. et al. Unusual angular dependence of the Raman response in black phosphorus. *ACS Nano* **9**, 4270–4276 (2015).
7. Qiao, J., Kong, X., Hu, Z.-X., Yang, F. & Ji, W. High-mobility transport anisotropy and linear dichroism in few-layer black phosphorus. *Nat. Commun.* **5**, 4475 (2014).
8. Tan, D. et al. Anisotropic optical and electronic properties of two-dimensional layered germanium sulfide. *Nano Research* **10**, 546–555 (2017).
9. Kong, W. et al. Angle resolved vibrational properties of anisotropic transition metal trichalcogenide nanosheets. *Nanoscale* **9**, 4175–4182 (2017).
10. Song, H. et al. Highly anisotropic Sb2Se3 nanosheets: gentle exfoliation from the bulk precursors possessing 1D crystal structure. *Adv. Mater.* **29**, 1700441 (2017).
11. Nemilentsau, A., Low, T. & Hanson, G. Anisotropic 2D materials for tunable hyperbolic plasmonics. *Phys. Rev. Lett.* **116**, 066804 (2016).
12. Yang, S. X. et al. High-performance few-layer Mo-doped ReSe2 nanosheet photodetectors. *Sci. Rep.* **4**, 6 (2014).
13. Yang, S. X. et al. Layer-dependent electrical and optoelectronic responses of ReSe2 nanosheet transistors. *Nanoscale* **6**, 7226–7231 (2014).
14. Liu, F. et al. Highly sensitive detection of polarized light using anisotropic 2D ReS2. *Adv. Funct. Mater.* **26**, 1169–1177 (2016).
15. Liu, E. et al. High responsivity phototransistors based on few-layer ReS2 for weak signal detection. *Adv. Funct. Mater.* **26**, 1938–1944 (2016).
16. Liu, E. et al. Integrated digital inverters based on two-dimensional anisotropic ReS2 field-effect transistors. *Nat. Commun.* **6**, 6991 (2015).
17. Wang, L. et al. Layered rhenium sulfide on free-standing three-dimensional electrodes is highly catalytic for the hydrogen evolution reaction: Experimental and theoretical study. *Electrochem. Commun.* **63**, 39–43 (2016).
18. Qi, F. et al. Self-assembled chrysanthemum-like microspheres constructed by few-layer ReSe2 nanosheets as a highly efficient and stable electrocatalyst for hydrogen evolution reaction. *Electrochim. Acta* **224**, 593–599 (2017).
19. Byunggil, K., Youngchan, K., Jeong Ho, C. & Changgu, L. Ambipolar transport based on CVD-synthesized ReSe2. *2D Mater.* **4**, 025014 (2017).
20. Xu, K. et al. Sulfur vacancy activated field effect transistors based on ReS2 nanosheets. *Nanoscale* **7**, 15757–15762 (2015).
21. Wang, X. et al. Enhanced rectification, transport property and photocurrent generation of multilayer ReSe2/MoS2 p–n heterojunctions. *Nano Res.* **9**, 507–516 (2016).
22. Kertesz, M. & Hoffmann, R. Octahedral vs trigonal-prismatic coordination and clustering in transition-metal dichalcogenides. *J. Am. Chem. Soc.* **106**, 3453–3460 (1984).
23. Lamfers, H. J., Meetsma, A., Wiegers, G. A. & deBoer, J. L. The crystal structure of some rhenium and technetium dichalcogenides. *J. Alloys Compd.* **241**, 34–39 (1996).
24. Tongay, S. et al. Monolayer behaviour in bulk ReS2 due to electronic and vibrational decoupling. *Nat. Commun.* **5**, 3252 (2014).
25. Liu, F. C. et al. Optoelectronic properties of atomically thin ReSSe with weak interlayer coupling. *Nanoscale* **8**, 5826–5834 (2016).
26. Zhao, H. et al. Interlayer interactions in anisotropic atomically thin rhenium diselenide. *Nano Res.* **8**, 3651–3661 (2015).
27. Biswas, D. et al. Narrow-band anisotropic electronic structure of ReS2. *Phys. Rev. B* **96**, 085205 (2017).
28. Webb, J. L. et al. Electronic band structure of ReS2 by high-resolution angle-resolved photoemission spectroscopy. *Phys. Rev. B* **96**, 115205 (2017).
29. Hart, L. S. et al. Electronic bandstructure and van der Waals coupling of ReSe2 revealed by high-resolution angle-resolved photoemission spectroscopy. *Sci Rep* **7**, 5145 (2017).
30. Gehlmann, M. et al. Direct observation of the band gap transition in atomically thin ReS2. *Nano Lett.* **17**, 5187–5192 (2017).
31. Tongay, S. et al. Monolayer behaviour in bulk ReS2 due to electronic and vibrational decoupling. *Nat. Commun.* **5**, 3252 (2014).
32. Ho, C. H., Huang, Y. S., Liao, P. C. & Tiong, K. K. Crystal structure and band-edge transitions of ReS2-xSex layered compounds. *J. Phys. Chem. Solids* **60**, 1797–1804 (1999).
33. Huang, Y. S., Ho, C. H., Liao, P. C. & Tiong, K. K. Temperature dependent study of the band edge excitons of ReS2 and ReSe2. *J. Alloys Compd.* **262**, 92–96 (1997).
34. Ho, C. H., Huang, Y. S., Tiong, K. K. & Liao, P. C. Absorption-edge anisotropy in ReS2 and ReSe2 layered semiconductors. *Phys. Rev. B* **58**, 16130–16135 (1998).
35. Gutierrez-Lezama, I., Reddy, B. A., Ubrig, N. & Morpurgo, A. F. Electroluminescence from indirect band gap semiconductor ReS2. *2d Mater.* **3**, 045016 (2016).
36. Aslan, O. B., Chenet, D. A., van der Zande, A. M., Hone, J. C. & Heinz, T. F. Linearly polarized excitons in single- and few-layer ReS2 crystals. *ACS Photonics* **3**, 96–101 (2016).
37. Ho, C.-H., Liu, Z.-Z. & Lin, M.-H. Direct and indirect light emissions from layered ReS2− xSex (0 ≤ x ≤ 2). *Nanotechnology* **28**, 235203 (2017).
38. Mann, J. et al. 2-Dimensional transition metal dichalcogenides with tunable direct band gaps: MoS2(1-x)Se2x monolayers. *Adv. Mater.* **26**, 1399–1404 (2014).
39. Yuan, H. T. et al. Evolution of the valley position in bulk transition-metal chalcogenides and their monolayer limit. *Nano. Lett.* **16**, 4738–4745 (2016).
40. Ho, C. H., Huang, Y. S., Chen, J. L., Dann, T. E. & Tiong, K. K. Electronic structure of ReS2 and ReSe2 from first-principles calculations, photoelectron spectroscopy, and electrolyte electroreflectance. *Phys. Rev. B* **60**, 15766–15771 (1999).
41. Dresselhaus, G. Spin-orbit coupling effects in zinc blende structures. *Phys. Rev.* **100**, 580–586 (1955).
42. Ho, C. H., Huang, Y. S., Liao, P. C. & Tiong, K. K. Piezoreflectance study of band-edge excitons of ReS2-xSex single crystals. *Phys. Rev. B* **58**, 12575–12578 (1998).
43. Wen, W. et al. Anisotropic spectroscopy and electrical properties of 2D ReS2(1-x) Se2x alloys with distorted 1T structure. *Small.* **13**, 1603788 (2017).
44. Kawashima, Y. & Katagiri, G. Observation of the out-of-plane mode in the Raman scattering from the graphite edge plane. *Phys. Rev. B* **59**, 62–64 (1999).
45. Kong, D. S. et al. Synthesis of MoS2 and MoSe2 films with vertically aligned layers. *Nano. Lett.* **13**, 1341–1347 (2013).
46. Wang, G. et al. In-plane propagation of light in transition metal dichalcogenide monolayers: optical selection rules. *Phys. Rev. Lett.* **119**, 047401 (2017).
47. Wolverson, D. & Hart, L. S. Lattice dynamics of the rhenium and technetium dichalcogenides. *Nanoscale Res. Lett.* **11**, 1–6 (2016).
48. Wolverson, D., Crampin, S., Kazemi, A. S., Ilie, A. & Bending, S. J. Raman spectra of monolayer, few-layer, and bulk ReSe2: An anisotropic layered semiconductor. *ACS Nano* **8**, 11154–11164 (2014).
49. Hart, L., Dale, S., Hoye, S., Webb, J. L. & Wolverson, D. Rhenium dichalcogenides: layered semiconductors with two vertical orientations. *Nano Lett.* **16**, 1381–1386 (2016).
50. Mitra, B., Gao, X., Wachs, I. E., Hirt, A. & Deo, G. Characterization of supported rhenium oxide catalysts: effect of loading, support and additives. *Phys. Chem. Chem. Phys.* **5**, 1144–1152 (2001).
51. Peterson, D., Petrou, A., Giriat, W., Ramdas, A. & Rodriguez, S. Raman scattering from the vibrational modes in Zn1-xMnxTe. *Phys. Rev. B* **33**, 1160 (1986).
52. Jadczak, J. et al. Composition dependent lattice dynamics in MoSxSe(2−x) alloys. *J. Appl. Phys.* **116**, 193505 (2014).
53. Dumcenco, D. O., Kobayashi, H., Liu, Z., Huang, Y. S. & Suenaga, K. Visualization and quantification of transition metal atomic mixing in Mo1-xWxS2 single layers. *Nat. Commun.* **4**, 1351 (2013).

54. Chanchal & Garg, A. K. MREI-model calculations for layered mixed crystals of the series HfS$_{2-x}$Te$_x$ (0 < = x < = 2). *Indian J. Pure Appl. Phys.* **46**, 330–333 (2008).

55. Chanchal & Garg, A. K. MREI-model calculations of Raman-active modes in layered mixed crystals TiS2-xSex (0 < = x < = 2). *J. Raman Spectrosc.* **39**, 115–118 (2008).

56. Sekine, T., Izumi, M., Nakashizu, T., Uchinokura, K. & Matsuura, E. Raman scattering and infrared reflectance in 2H-MoSe2. *J. Phys. Soc. Jpn.* **49**, 1069–1077 (1980).

57. Mitioglu, A. et al. Second-order resonant Raman scattering in single-layer tungsten disulfide WS 2. *Phys. Rev. B* **89**, 245442 (2014).

58. Pimenta, M. A., del Corro, E., Carvalho, B. R., Fantini, C. & Malard, L. M. Comparative study of Raman spectroscopy in graphene and MoS$_2$-type transition metal dichalcogenides. *Acc. Chem. Res.* **48**, 41–47 (2014).

59. Lee, J.-U., Park, J., Son, Y.-W. & Cheong, H. Anomalous excitonic resonance Raman effects in few-layered MoS$_2$. *Nanoscale* **7**, 3229–3236 (2015).

60. Cakir, D., Sahin, H. & Peeters, F. M. Doping of rhenium disulfide monolayers: a systematic first principles study. *Phys. Chem. Chem. Phys.* **16**, 16771–16779 (2014).

61. Davis, S. Photoemission studies of rhenium disulfide oxidation: Altered core-level structure and reactivity of defect sites. *Catal. Lett.* **2**, 1–7 (1989).

62. Shim, J. et al. High-performance 2D rhenium disulfide (ReS$_2$) transistors and photodetectors by oxygen plasma treatment. *Adv. Mater.* **28**, 6985–6992 (2016).

63. Stachiotti, M., Corà, F., Catlow, C. & Rodriguez, C. First-principles investigation of ReO$_3$ and related oxides. *Phys. Rev. B* **55**, 7508 (1997).

64. Purans, J., Purans, A., Kuzmin, E., Cazzanelli, G. & Mariotto Disorder-induced Raman scattering in rhenium trioxide (ReO$_3$). *J. Phys. Condens. Matter.* **19**, 226206 (2007).

65. Beattie, I. R. & Ozin, G. A. Vibrational spectrum of gaseous, liquid, and solid Re$_2$O$_7$. *J. Chem. Soc. A*, 2615–2619, (1969).

66. Lacheen, H. S., Cordeiro, P. J. & Iglesia, E. Isolation of rhenium and ReOx species within ZSM5 channels and their catalytic function in the activation of alkanes and alkanols. *Chem. Eur. J.* **13**, 3048–3057 (2007).

67. Davis, S. & Carver, J. Oxygen chemisorption at defect sites in MoS$_2$ and ReS$_2$ basal plane surfaces. *Appl. Surf. Sci.* **20**, 193–198 (1984).

68. KC, S., Longo, R. C., Wallace, R. M. & Cho, K. Surface oxidation energetics and kinetics on MoS$_2$ monolayer. *J. Appl. Phys.* **117**, 135301 (2015).

69. Huang, T. P., Lin, D. Y., Kao, Y. C., Wu, J. D. & Huang, Y. S. Polarized thermoreflectance and reflectance study of ReS$_2$ and ReS$_2$:Au single crystals. *Jpn. J. Appl. Phys.* **50**, 04DH17 (2011).

70. Giannozzi, P. et al. QUANTUM ESPRESSO: a modular and open-source software project for quantum simulations of materials. *J. Phys. Condens. Matter* **21**, 395502 (2009).

71. Lazzeri, M. & Mauri, F. First-principles calculation of vibrational raman spectra in large systems: signature of small rings in crystalline SiO$_2$. *Phys. Rev. Lett.* **90**, 036401 (2003).

72. Perdew, J. P. & Zunger, A. Self-interaction correction to density-functional approximations for many-electron systems. *Phys. Rev. B* **23**, 5048–5079 (1981).

73. Monkhorst, H. J. & Pack, J. D. Special points for Brillouin-zone integrations. *Phys. Rev. B* **13**, 5188–5192 (1976).

74. Rice, C. et al. Raman-scattering measurements and first-principles calculations of strain-induced phonon shifts in monolayer MoS$_2$. *Phys. Rev. B* **87**, 081307 (2013).

75. Wang, F. et al. Strain-induced phonon shifts in tungsten disulfide nanoplatelets and nanotubes. *2D Mater.* **4**, 015007 (2016).

76. Kokalj, A. Computer graphics and graphical user interfaces as tools in simulations of matter at the atomic scale. *Comput. Mater. Sci.* **28**, 155–168 (2003).

77. Chenet, D. A. et al. In-plane anisotropy in mono- and few-layer ReS$_2$ probed by raman spectroscopy and scanning transmission electron microscopy. *Nano. Lett.* **15**, 5667–5672 (2015).

78. McCreary, A. et al. Intricate resonant raman response in anisotropic ReS$_2$. *Nano Lett.* **17**, 5897 (2017).

79. Lorchat, E., Froehlicher, G. & Berciaud, S. Splitting of interlayer shear modes and photon energy dependent anisotropic raman response in n-layer ReSe$_2$ and ReS$_2$. *ACS Nano* **10**, 2752–2760 (2016).